ADVANCED FUNCTIONAL MATERIALS
www.afm-journal.de

# Designing Fe-Based Amorphous Alloys With both Ultra-High Magnetization and Ultra-Low Coercivity Through Artificial Intelligence

*Shiyu Yang, Bowen Zang, Mingliang Xiang, Fayuan Shen, Lijian Song, Meng Gao, Yan Zhang, Juntao Huo,* and Jun-Qiang Wang**

**Designing soft magnetic alloys with high magnetization and low coercivity is of special interest for application in high-frequency and high-power electric and electronic components. In this work, high-precision machine-learning models based on 536 different Fe-based amorphous alloys are developed. It reveals that the electronegativity difference ($\delta_\chi$) and mixing enthalpy ($\Delta H_{mix}$) of the alloying elements play critical roles in determining the saturated magnetization ($B_s$) of amorphous alloys. Specifically, smaller $\delta_\chi$ can strengthen the biased distribution of spin-up and spin-down electrons as is revealed by ab initio simulations. Based on these findings, a series of advanced amorphous/nanocrystalline alloys with $B_s$ higher than 1.90 T and coercivity ($H_c$) as low as 1.2 A m$^{-1}$ are designed, which also have good amorphous forming ability owing to the suitable mixing enthalpy. The designed alloys with high $B_s$ and low $H_c$ hold promising application potentials in electronic components of high power density and low energy loss.**

## 1. Introduction

Soft magnetic materials are pivotal in energy transmission and conversion within electrical and electronic systems.[1] In response to the increasingly severe global energy challenges, there is an imperative shift in modern electronic devices toward miniaturization, higher operating frequencies, and enhanced energy efficiency.[2] In this milieu, the development of materials with exceptional soft magnetic properties is critical to facilitate these advancements. Specifically, there is an urgent demand for soft magnetic materials that combine high saturated magnetization ($B_s$) and low coercivity ($H_c$), which is essential to satisfy the dual requirements of high power density, low loss, and the miniaturization of devices.[3] For decades, Fe-based amorphous/nanocrystalline alloys have emerged as the most promising candidate alloys for addressing this challenge due to their excellent soft magnetic properties.[4] Surpassing traditional materials such as silicon steel with $H_c$ of ≈40 A m$^{-1}$, Fe-based amorphous alloys demonstrate a significant decrease in core loss and $H_c$ that is usually lower than 10 A m$^{-1}$, thereby enabling devices to efficiently operate at frequencies up to 10 kHz without sacrificing energy efficiency or generating excessive heat.[5] However, the $B_s$ of Fe-based amorphous/nanocrystalline alloys are usually between 1.2–1.7 T which is lower than silicon steels of 1.8–2.0 T, which restricts their application in high-power density equipment.[6] Therefore, designing new amorphous/nanocrystalline alloys with high $B_s$ and low $H_c$ is imperative for the subsequent advancements in device performance and energy efficiency.[7]

Historically, the development of Fe-based amorphous alloys has relied on trial-and-error methods, devoid of substantial theoretical underpinning.[4,8] This conventional approach has notably impeded the efficient advancement of high $B_s$ amorphous alloys. The recent upsurge in machine learning (ML) applications within the realm of materials science is catalyzing a transformative shift.[9] ML has powerful potential in data-driven, offering a more efficient pathway for the accelerated discovery of novel materials, particularly in the realm of complex disordered materials.[10]

In this work, we established three distinct ML models to accurately predict the $B_s$ of Fe-based amorphous alloys. Employing Shapley Additive exPlanations (SHAP) analysis,[11] we propose practical guidelines for the design of high $B_s$ Fe-based amorphous/nanocrystalline alloys, specifying the optimal ranges for critical parameters including Fe content ($C_{Fe}$), mixing enthalpy ($\Delta H_{mix}$), and electronegativity difference ($\delta_\chi$). Following these data-driven guidelines, we have designed Fe-based amorphous/nanocrystalline alloys with ultrahigh $B_s$ of 1.92 T. Our findings highlight the significance of $\delta_\chi$ as a pivotal indicator for the $B_s$ in Fe-based amorphous alloys, a factor previously

S. Yang, B. Zang, M. Xiang, F. Shen, L. Song, M. Gao, Y. Zhang, J. Huo, J.-Q. Wang
Key Laboratory of Magnetic Materials and Devices
and Zhejiang Province Key Laboratory of Magnetic Materials and Application Technology
Ningbo Institute of Materials Technology and Engineering
Chinese Academy of Sciences
Ningbo 315201, China
E-mail: huojuntao@nimte.ac.cn; jqwang@nimte.ac.cn
S. Yang, Y. Zhang, J. Huo, J.-Q. Wang
Center of Materials Science and Optoelectronics Engineering
University of Chinese Academy of Sciences
Beijing 100049, China

The ORCID identification number(s) for the author(s) of this article can be found under https://doi.org/10.1002/adfm.202425588

**DOI: 10.1002/adfm.202425588**

 

**Table 1.** Parameters calculated from alloy composition as candidate features.

| Features | Denotation and Formula |
|---|---|
| Atomic concentration | $C_i$, $i$ = Fe, Co, Ni, B, … |
| Valence electron concentration | $VEC = \sum C_i\, VEC_i$ |
| Mean atomic radius | $\bar{r} = \sum C_i r_i$ |
| Average electronegativity | $\bar{\chi} = \sum C_i \chi_i$ |
| Electronegativity difference | $\delta_\chi = \sum C_i \lvert\chi_i - \bar{\chi}\rvert$ |
| Entropy of mixing | $\Delta S_{mix} = \sum -RC_i ln(C_i)$ |
| Mixing enthalpy | $\Delta H_{mix} = \sum 4C_i C_{j\neq} \Delta H_{ij}^{mix}$ |

underemphasized. Further, first-principles calculations revealed that, at consistent iron concentrations, Fe-based amorphous alloys with minimized $\delta_\chi$ yield a higher $B_s$. This occurs because a smaller $\delta_\chi$ can maintain the Fermi level of the alloy at a lower level, thereby maintaining or even increasing the number of unpaired electrons in the iron atom, exhibiting a larger total magnetic moment.

## 2. Results and Discussions

In the data mining phase, we collected data from 536 different Fe-based amorphous alloys from the literature to construct an initial dataset. All the collected data are documented in the Supporting Information. Figure S1a (Supporting Information) shows the compositional diversity within these alloys along with the $B_s$ distribution. This study encompasses a dataset of 536 Fe-based amorphous alloys including 20 different alloying elements and $B_s$ values ranging from 0.33 to 1.92 T. Six extra input features were generated from the initial dataset through Matminer software,[12] as outlined in **Table 1**. The correlation between each pair of input features (X, Y) was assessed by their Pearson correlation coefficient (PCC), calculated using Equation (1).

$$\rho_{(X,Y)} = \frac{cov\,(X, Y)}{\sigma_X \sigma_Y} \tag{1}$$

In Equation (1), cov(X, Y) signifies the covariance of continuous variables $X$ and $Y$, while $\sigma_X$ represents the standard deviation of variable X. The PCC of different pairs of input features is shown in Figure S1b (Supporting Information). A pair of features with an absolute PCC nearing unity represents a strong linear correlation between them. Such a correlation suggests that one feature in the pair should be substituted by the other to streamline model complexity and prevent overfitting.[13] Considering this features such as $\Delta S_{mix}$, $C_C$, $C_P$, and $\chi$ were excluded from the initial dataset due to their high absolute PCC values—exceeding 0.80—with $C_{Fe}$, $\delta_\chi$-$C_C$, $\delta_\chi$-$\bar{\chi}$, $\bar{\chi}$-$C_P$, and $C_P$-$C_B$, respectively. This strategic refinement of the dataset paved the way for a more accurate and efficient machine-learning process.[14]

Three distinct ML algorithms were applied to predict the $B_s$ of Fe-based amorphous alloys while concurrently exploring the relationship between the input features and the predictive target. These three ML algorithms include XGBoost,[15] Random Forest (RF),[16] and Support Vector Machine (SVM).[17] The detailed training and optimization process of the machine learning model can be found in the methods section. **Figure 1**a–c schematically shows the predictive performance of the abovementioned three ML models, both on the training set and the test set. In order to comprehensively gauge the performance of each model, we computed two distinct loss functions, the Root Mean Square Error (RMSE) and the determination coefficient ($R^2$) from the test set output.

$$RMSE = \sqrt{\frac{1}{n}\sum_{i=1}^{n}\left(y_i - \hat{y}_i\right)^2} \tag{2}$$

$$R^2 = 1 - \frac{\Sigma_{i=0}^{n}\left(y_i - \hat{y}_i\right)^2}{\Sigma_{i=0}^{n}\left(y_i - \bar{y}_i\right)^2} \tag{3}$$

where $y_i$ represents the true value of $B_s$ while $\hat{y}_i$ represents the predicted $B_s$. And $\bar{y}_i$ is the average of $y_i$. The smaller the RMSE the better the model fitting effect. And $R^2$ value lies between 0 and 1. The closer $R^2$ is to 1, the more accurate the model predicts. The $R^2$ coefficients of all three models are greater than 0.85,

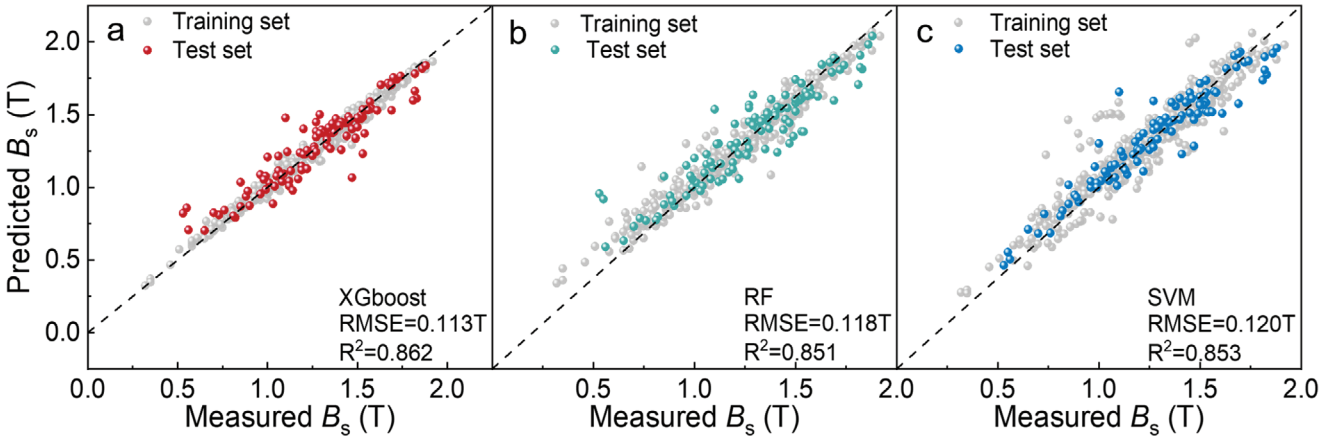


**Figure 1.** The predictive performance of three models. a) XGBoost, b) RF, c) SVM. The gray spheres and colored spheres represent the performance of the models in the training set and the test set, respectively. The dashed lines represent y = x. The root mean square error (RMSE) and $R^2$ parameter are listed in the figure.

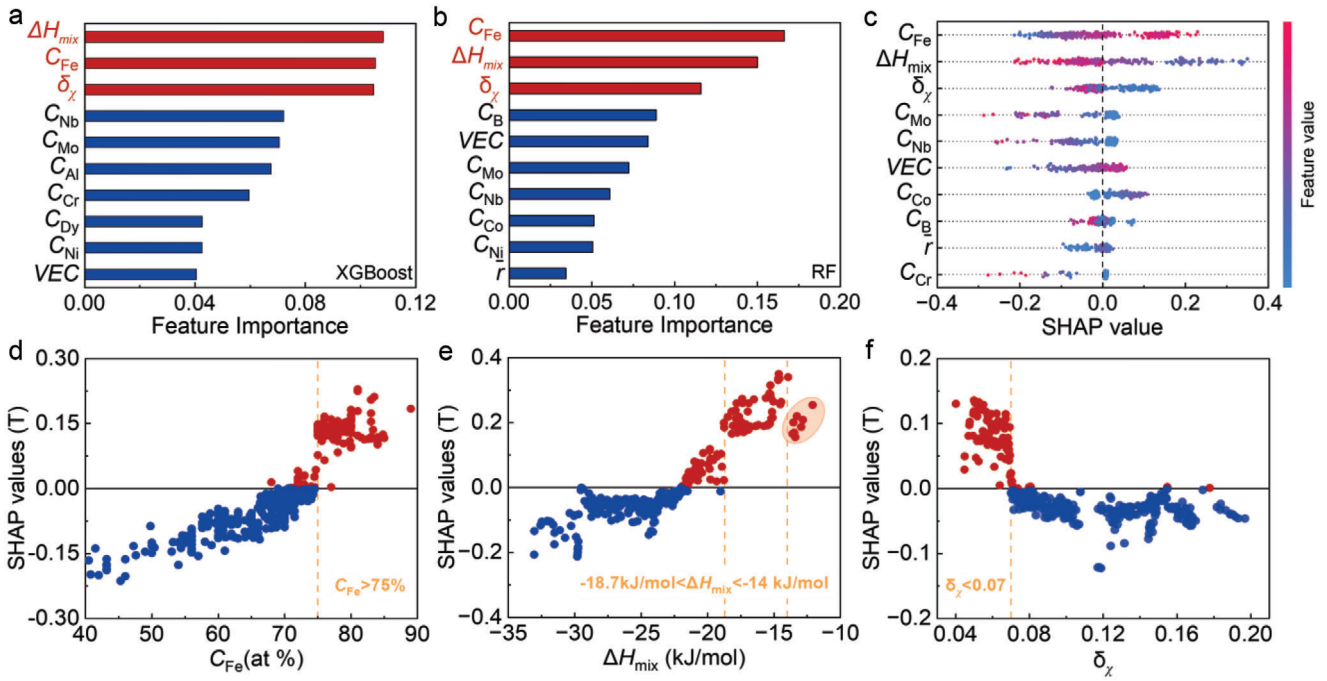


**Figure 2.** Feature importance and SHAP analysis for different machine learning models. The feature importance rankings of a) XGboost and b) RF models. $C_{Fe}$, $\Delta H_{mix}$, and $\delta_\chi$ are the top three important factors. c) The distribution of SHAP values for features. Each point represents a sample of iron based amorphous alloy. The color changes from blue to red, which denotes the feature's own value increases. The increase in SHAP value indicates a positive contribution to $B_s$. d,e,f, The SHAP value for $C_{Fe}$, $\Delta H_{mix}$, and $\delta_\chi$, respectively.

indicating that the predicted $B_s$ are very consistent with the experimentally measured $B_s$, and the root mean square error in the test set does not exceed 0.12. This indicates that the machine learning model we trained is effective and reliable for predicting $B_s$ in Fe-based amorphous alloys. Notably, the predictive data derived from the XGBoost model demonstrated the largest $R^2$ along with the smallest RMSE. These results collectively indicate the superior performance of the XGBoost model over the other two models.

XGBoost and RF models provide interpretable frameworks that elucidate the decision-making process of the algorithm, offering insights into the potential link between input features and the predicted $B_s$. The calculated value of Feature Importance (FI)[16] quantifies the influence of distinct features on the target predictions.[18] **Figure 2a** delineates the feature importance rankings for the XGBoost model, where $C_{Fe}$, $\Delta H_{mix}$, and $\delta_\chi$ emerge as the most influential features on $B_s$, a finding corroborated by the RF model analysis, illustrated in Figure 2b. To bolster the validity of FI evaluations and mitigate biases arising from singular methodological reliance, Permutation Importance (PI)[16,19] was employed as an auxiliary evaluative measure. PI imparts a secondary quantitative dimension to feature impact assessment by evaluating the reduction in model accuracy when the values of the features are randomly permuted. The consonance of PI rankings with FI, as depicted in Figure S2 (Supporting Information), reinforces the preestablished conclusions. An integrative analysis of the results from both FI and PI evaluations substantiates the criticality of these three features in predicting $B_s$ for both XGBoost and RF models.

In response to the paucity of investigations into the effects of $\Delta H_{mix}$ and $\delta_\chi$ on $B_s$, it is necessary for us to focus our next data mining work on how these two variables specifically affect $B_s$. We employed SHapley Additive exPlanations (SHAP)[20] to interpret how a single feature affects the output of the model. The SHAP value of the $i$-th feature is calculated by

$$\varphi_i = \sum_{S \subseteq F \setminus i} \frac{|S|!\,(|F| - |S| - 1)!}{|F|!} \left[ f_{S\cup\{i\}}\left(x_{S\cup\{i\}}\right) - f_S\left(x_S\right) \right] \quad (4)$$

where $F$ is the set of all features, $S$ is the subset of $F$, $S \cup \{i\}$ is the union of the subset $S$ and the $i$-th feature, $f_{S\cup\{i\}}\left(x_{S\cup\{i\}}\right)$ is the predicted value generated when the model considers the $i$-th feature, while $f_S(x_S)$ is the case when the $i$-th feature is not considered. So, the meaning of $f_{S\cup\{i\}}\left(x_{S\cup\{i\}}\right) - f_S\left(x_S\right)$ is the contribution of the $i$-th feature to the model output after being added to the feature subset. $\frac{|S|!(|F|-|S|-1)!}{|F|!}$ represents a weighted average for all possible differences. These values are instrumental in quantifying the extent to which each feature sways the model's forecast above or below an established baseline. As illustrated in Figure 2c, samples exhibiting large $\Delta H_{mix}$ tend to manifest positive SHAP values, while those with small $\Delta H_{mix}$ display negative SHAP values. This observation suggests that a larger $\Delta H_{mix}$ tends to contribute positively to the predicted $B_s$ of amorphous alloys and vice versa. Conversely, a smaller $\delta_\chi$ is advantageous for predicting an enhanced $B_s$, displaying an inverse relationship compared to $\Delta H_{mix}$. Figure 2d–f shows the distribution of SHAP values to determine the critical thresholds. It is observed that with the increment in $C_{Fe}$ and $H_{mix}$, there is a progressive transition of SHAP

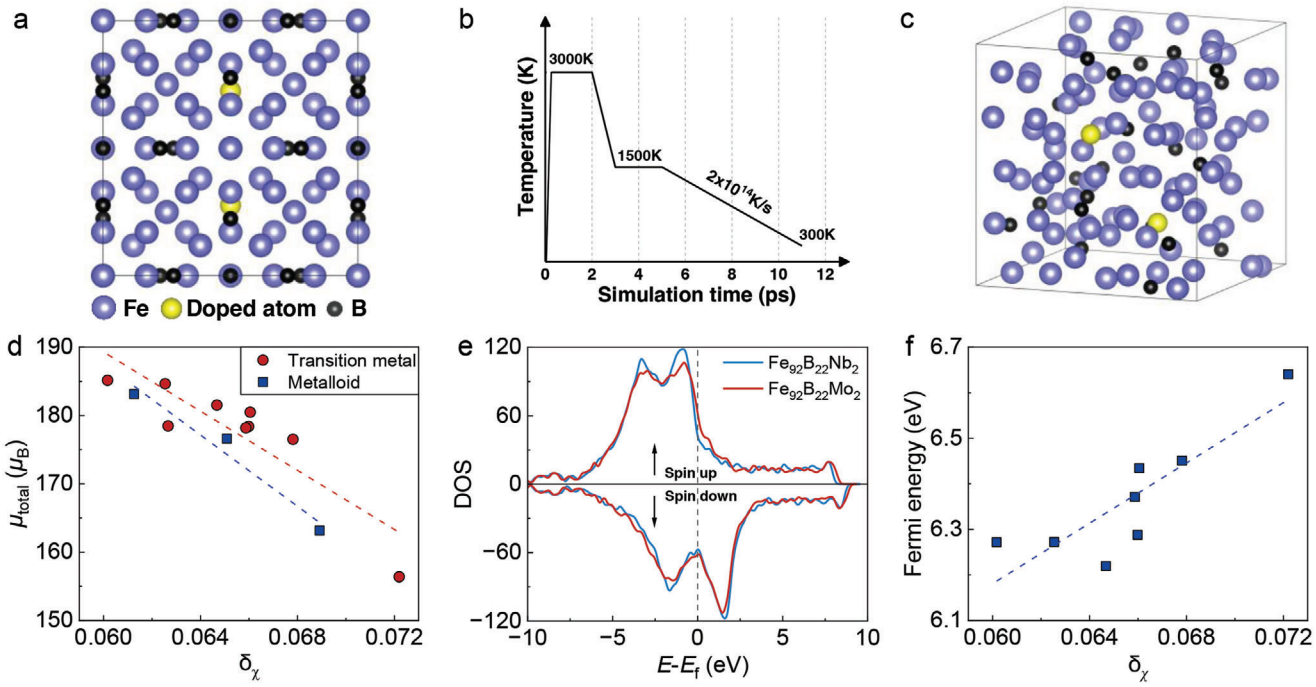


**Figure 3.** Calculation of the magnetic properties of alloys doped with different elements. a) Crystal structure modeling of Fe-B-X alloys with doped atoms. b) The formation process of amorphous alloys simulated by ab initio molecular dynamics. c) The structure of Fe-B-X amorphous alloys formed by quenching. d, The dependence of total magnetic moment ($\mu_{total}$) of alloy on $\delta_\chi$. The red dots represent alloys doped with transition metal elements, i.e., $Fe_{92}B_{22}X_2$ and $Fe_{92}B_{20}X_4$ alloys, where X = Zr, Nb, Mo, Al, Ga. Blue squares represent $Fe_{92}B_{24}$, $Fe_{92}B_{22}Si_2$, and $Fe_{92}B_{22}Si_4$. e) The density of states (DOS) for $Fe_{92}B_{22}Nb_2$ ($\delta_\chi = 0.066$) and $Fe_{92}B_{22}Mo_2$ ($\delta_\chi = 0.072$) alloys. The dashed line represents Fermi energy. f) The Fermi energy of the alloy shows an upward trend with the increase of $\delta_\chi$.

values from the negative to the positive domain, indicating a pivotal shift from diminishing to bolstering $B_s$. The points of this transition are discerned at 75 at.% for $C_{Fe}$ and −18.7 kJ mol$^{-1}$ for $\Delta H_{mix}$.

Notably, the circled points in Figure 2e show a decline in the upward trend of SHAP values when $\Delta H_{mix}$ exceeds -14 kJ/mol, indicating a reduced contribution to $B_s$. Although $\Delta H_{mix}$ remains favorable for $B_s$ in this range, it weakens the glass-forming ability. Therefore, $\Delta H_{mix}$ between -18.7 and −14 kJ mol$^{-1}$ should be an optimal balance for high $B_s$ and good glass-forming ability. For $\delta_\chi$ less than 0.07, the SHAP value rapidly decreases as $\delta_\chi$ increases and tends to stabilize when $\delta_\chi$ is greater than 0.07. It indicates that a smaller $\delta_\chi$ is more favorable for achieving high $B_s$. Consequently, a reasonable criterion can be established based on these findings to guide the efficient design of Fe-based amorphous alloys with superior $B_s$. These criteria require that $C_{Fe}$ should exceed 75.%, $\Delta H_{mix}$ needs to be within the range of −18.7 to −14 kJ mol$^{-1}$, and $\delta_\chi$ should be less than 0.07.

The relationship between the $\Delta H_{mix}$ and $B_s$ can be understood as an intermediate bridge to balance the amorphous formation ability. Previous studies[21] have shown that alloys with a higher negative mixing enthalpy exhibit good amorphous-forming ability. Therefore, a suitable mixing enthalpy benefits both $B_s$ and amorphous-forming ability. However, the physical basis for the negative correlation between $\delta_\chi$ and $B_s$ is relatively unexplored in prior studies. Thus, to unravel the reliability of this discovery, ab initio molecular dynamics simulations were utilized to simulate the formation of amorphous $Fe_{92}B_{22}X_2$ and $Fe_{92}B_{20}X_4$ alloys (where X = Zr, Nb, Mo, Al, Ga, Si, B). **Figure 3a** illustrates the process of an alloy transitioning from a crystalline state to an amorphous glassy state through melting and subsequent quenching, as revealed by ab initio molecular dynamics simulations. A more detailed methodology of the simulation process is provided in the methods section. Figure S3 (Supporting Information) presents the pair distribution function $g_{(r)}$ of Fe-Fe atoms in alloys doped with various elements. The observed $g_{(r)}$ curves are characterized by an absence of periodic peaks. The first peak is observed consistently between 2.46 to 2.52 Å across all samples. A particularly notable feature is the splitting observed in the second peak, which is a deviation from the typical structure of a liquid state. This distinct splitting in the second peak is a critical indicator, affirming that the alloys synthesized via our simulation process have successfully achieved a well-defined amorphous structure.

As is well known, the $B_s$ of alloys are mainly attributed to the net magnetic moment of the ferromagnetic elements that make up the alloy.[22] The total magnetic moment ($\mu_{total}$) of the alloy doped with different elements was calculated by first-principles calculation. As shown in Figure 3b, after doping transition metal elements or metalloid elements, the $\mu_{total}$ of the alloy shows a significant decreasing trend as the $\delta_\chi$ increases. This result indicates that, while the iron content remains the same, a smaller $\delta_\chi$ makes iron atoms exhibit larger magnetic moments, thereby increasing the $B_s$ of the alloy.

The magnetic moment of an iron atom is mainly determined by the number of unpaired electrons. Thus, the $\mu_{total}$ could be expressed as (N↑-N↓) $\mu_B$, where N↑ and N↓ are the numbers of

up-spin and down-spin valence electrons, respectively; $\mu_B$ represents the Bohr magneton. Figure 3c compares the total density of states for $Fe_{92}B_{22}Nb_2$ ($\delta_\chi = 0.066$, $E_f = 6.43$, $\mu_{total} = 180.49\mu_B$) and $Fe_{92}B_{22}Mo_2$ ($\delta_\chi = 0.072$, $E_f = 6.64$, $\mu_{total} = 156.38\mu_B$) alloys. Due to the exchange interaction of electron spins, the density of states for spin up and spin down exhibits an asymmetric distribution near the Fermi level. In the region below the Fermi level, the $Fe_{92}B_{22}Nb_2$ alloy exhibits a significantly higher density of states for spin-up electrons compared to the $Fe_{92}B_{22}Mo_2$ alloy, while the spin-down electron density of states does not differ significantly. This indicates that doping Nb leads to a rearrangement of electron spins, resulting in relatively more spin-up electrons below the Fermi level and an increase in the number of unpaired electrons. Based on the rigid band model, during the doping process, as electrons are either added or removed, the Fermi level correspondingly ascends or descends until all additional electrons are encompassed below the new Fermi level.

As depicted in Figure 3d, the Fermi level increases with the increase of $\delta_\chi$. This trend indicates that the doping elements are introducing more extra electrons, resulting in a rise in the Fermi level. Therefore, the impact of $\delta_\chi$ on $B_s$ can be attributed to changes in Fermi energy levels. Before doping, the amorphous $Fe_{92}B_{24}$ alloy exhibits an initial $\delta_\chi$ of 0.0689, along with a specific distribution of electronic states. Below the Fermi level, the density of states for spin-up electrons exceeds that of spin-down electrons. When doping occurs – with the dopant atoms replacing boron atoms – and if the resulting alloy has a larger $\delta_\chi$ while maintaining the same number of iron atoms, this leads to an elevation of the Fermi level. Such an elevation results in more spin-down electrons occupying states below the Fermi level, implying that some electrons move into the 3D orbitals of Fe atoms to pair with unpaired electrons, thereby reducing the total number of unpaired electrons. Conversely, if doping leads to a lower $\delta_\chi$ in the alloy, it suggests a more even distribution of the ability to attract or donate electrons among atoms. In this scenario, the Fermi level tends to remain stable or even decrease. This stability or reduction can maintain or even increase the number of unpaired electrons. As a result, the alloy may exhibit a larger $\mu_{total}$. This relationship between the doping process, $\delta_\chi$, Fermi level changes, and the distribution of unpaired electrons is crucial for understanding and manipulating the magnetic properties of Fe-based amorphous alloys.

**Figure 4** shows the distribution of $B_s$ in dimensions of $\Delta H_{mix}$, $C_{Fe}$, and $\delta_\chi$ for the 536 alloys. It is evident that higher $B_s$ are mainly found in regions with higher Fe content and smaller $\delta_\chi$. In alignment with these guidelines, we designed 6 distinct Fe-based amorphous alloys with -14 kJ/mol $> \Delta H_{mix} > -15$ kJ mol$^{-1}$ and $0.04 < \delta_\chi < 0.065$. Additionally, due to the strong ferromagnetic exchange interaction between Co and Fe,[23] we substitute part of Fe with Co to enhance the alloy's $B_s$. The XRD patterns of the melt-spun ribbons of these alloys are presented in **Figure 5a**. All XRD patterns demonstrate a diffused peak at $2\theta$ = 44–45° representing a mostly amorphous structure. Figure 4b presents the DSC curves of the six alloys, with their crystallization temperatures ranging from ≈360 to 380 °C. Accordingly, subsequent annealing temperatures were set between 340 and 420 °C, with an annealing time of 15 min. A longitudinal external magnetic field of ≈400 A m$^{-1}$ is applied during annealing. The annealing can mitigate magneto anisotropy

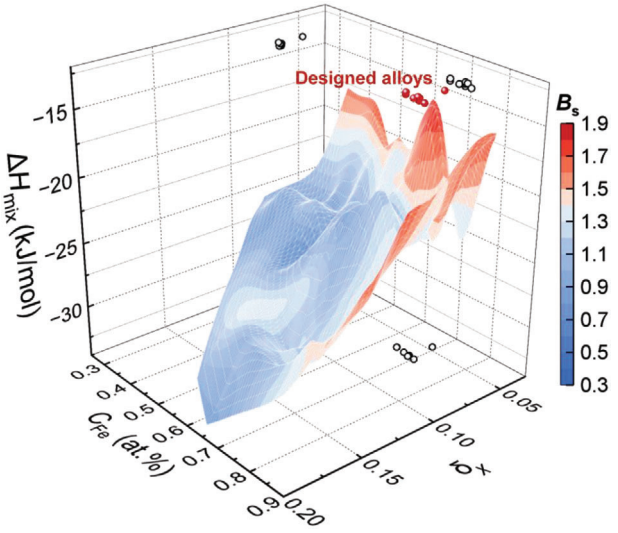


**Figure 4.** The distribution of $B_s$ for Fe-based amorphous alloys in the dimensions of $C_{Fe}$, $\Delta H_{mix}$ and $\delta_\chi$ space. The red spheres represent the alloys designed in this work, while the black open circle represent the projections on each 2D panel.

energy fluctuation caused by internal stresses, thus making the locally induced anisotropies coherent.[23a,24] Upon increasing the annealing temperature, the $H_c$ of the alloy exhibited an initial decline followed by an increase, suggesting an optimal annealing temperature at which $H_c$ was substantially reduced from a range of 13–27 to 1.2–5.6 A m$^{-1}$, as demonstrated in Figure 5c. The coercivity is much lower than crystalline silicon steels.

The magnetization curves of the annealed samples with the lowest $H_c$ are shown in Figure 5d. Each alloy exhibits a $B_s$ value exceeding 1.85 T, thereby affirming the effectiveness of our data-driven design strategy. Notably, the $(Fe_{82}Co_{18})_{85.5}Ni_{1.5}B_9P_3C_1$ and $Fe_{69}Co_{16}Ni_1Si_3B_{11}$ alloys exhibit ultrahigh $B_s$ of ≈1.92 T. The experimental $B_s$ values are in congruence with those predicted by machine learning, as depicted in Figure 1a. The bright-field TEM images and the selected-area electron diffraction pattern of a representative alloy, $(Fe_{82}Co_{18})_{85.5}Ni_{1.5}B_9P_3C_1$, are depicted in Figure 5e. As-spun ribbons reveal no discernible crystalline phases. The diffraction pattern is ring-like, confirming a long-range disordered atomic arrangement, typical of an amorphous structure. The annealed ribbons formed fine grains smaller than 20 nm within the amorphous matrix, reducing effective anisotropy and lowering $H_c$. The sparse grain distribution further weakens grain boundary pinning, enabling the $(Fe_{82}Co_{18})_{85.5}Ni_{1.5}B_9P_3C_1$ alloy to achieve high $B_s$ with low coercivity. Figure 5f compares the $B_s$ and $H_c$ values for various iron-based amorphous and nanocrystalline alloys.[23a,25] The amorphous/nanocrystalline alloy developed in this study achieves a $B_s$ notably superior to that of the majority of conventional nanocrystalline and cobalt-containing amorphous alloys. Additionally, its low coercivity is comparable to that of the extensively applied Finemet-type nanocrystalline alloys.

In this work, although the current model and compositional design criteria primarily focus on Fe-based alloys, the

 

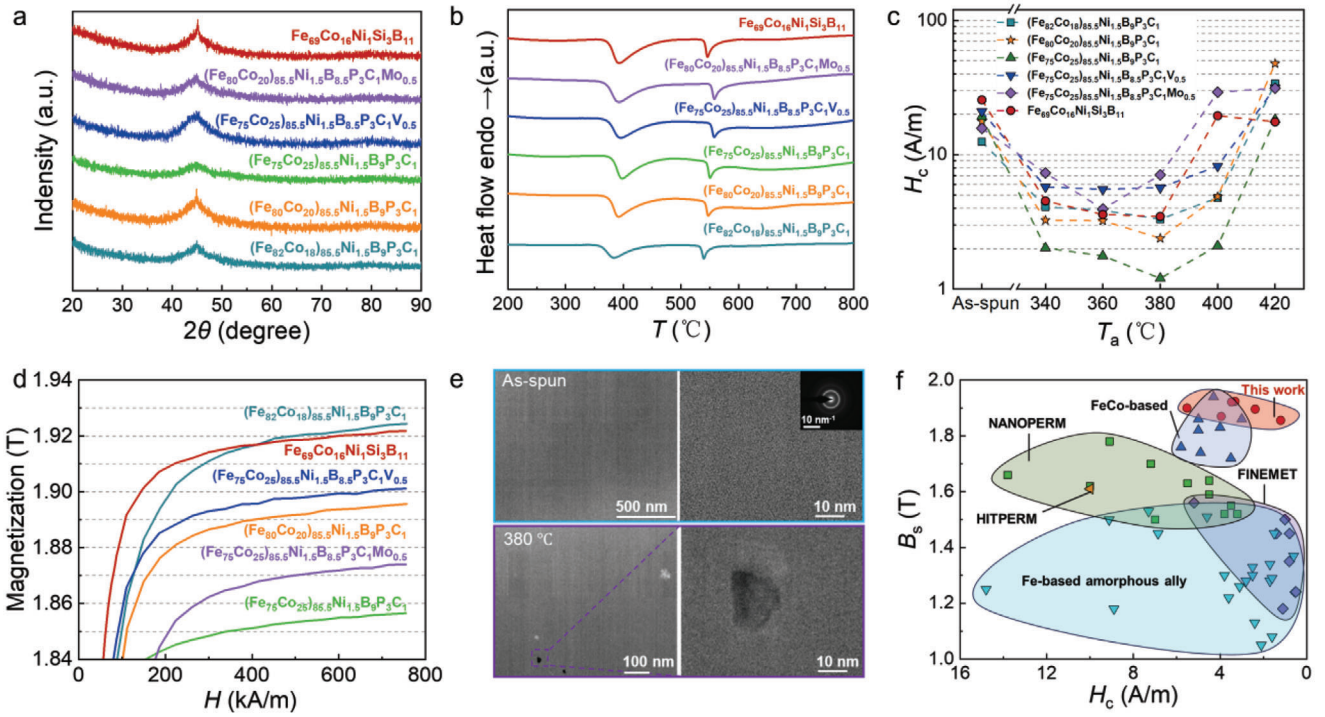


**Figure 5.** Properties of designed Fe-based alloys with desirable $\Delta H_{mix}$ and $\delta_{\chi}$. a) The XRD patterns of the melt-spun ribbons. b) The DSC curves of the melt-spun ribbons. c) The variation of coercivity with annealing temperature. d) The magnetization curves of samples annealed at optimal temperature. e) The bright-field TEM image and the selected-area electron diffraction pattern of $(Fe_{82}Co_{18})_{85.5}Ni_{1.5}B_9P_3C_1$. f) The comparison of $B_s$ and $H_c$ of soft magnetic Fe-based amorphous/nanocrystalline alloys.

generalization capability of the model is expected to be significantly enhanced by expanding the dataset to include more non-Fe-based alloy systems, such as Co-based and Ni-based alloys, and by extracting more universal physical parameters through feature engineering. This will facilitate the development of a generalized model applicable to multiple alloy systems. Furthermore, integrating advanced methods such as cross-system data consolidation and transfer learning will further improve the adaptability and predictive accuracy of the model across different alloy systems.

## 3. Conclusion

We have successfully developed three machine learning models to predict advanced Fe-based amorphous alloys with high $B_s$. Three key factors, e.g. $C_{Fe}$, $\Delta H_{mix}$, and $\delta_{\chi}$ are identified that exhibit a close relationship with the $B_s$. First-principles simulations further support this finding. Specifically, when the iron content is held constant, iron-based amorphous alloys with smaller $\delta_{\chi}$ tend to have more unpaired electrons in the iron atoms and increase the alloy's total magnetic moment. Based on the established criteria, three distinct alloy systems, Fe-Co-Ni-Si-B, Fe-Co-Ni-B-P-C, and Fe-Co-N-B-P-C-V, have all achieved high $B_s$ exceeding 1.90 T, highlighting the broad applicability and effectiveness of our design strategy across different compositions. Additionally, under magnetic field annealing, the coercivity $H_c$ can be reduced to as low as 1.2 A/m. The combination of ultra-high $B_s$ and extremely low $H_c$ makes the alloys have promising application potential.

## 4. Experimental Section

*The Training Process of Machine Learning Models*: To initiate the machine learning process, a comprehensive dataset was first compiled by extracting necessary physical features from the initial dataset. This dataset was partitioned into a training set and a test set with an 8:2 ratio. The training set was used to optimize the hyperparameters of each ML algorithm by employing a random search method and minimizing the root mean square error RMSE of model output. The test set serves to evaluate its predictive accuracy. Throughout the training and optimization phases, a 5-fold cross-validation was implemented to ensure the robustness and reliability of the model.

The machine learning code for this study was developed using the scikit-learn[26] framework in Python. Additionally, the physical parameters of the alloys included in the dataset were calculated using Matminer,[12] a tool designed for materials data mining.

*Sample Preparation*: The alloy ingots were synthesized by arc melting a mixture of high-purity elements: Fe (99.99 wt.%), Co (99.95 wt.%), Ni (99.99 wt.%), Si (99.99 wt.%), B (99.99 wt.%), and $Fe_3P$ (99.5 wt.%) under an argon atmosphere. Ribbon samples, ≈0.8 mm in width and 22–25 µm in thickness were produced using a single-roller melt spinning technique, with the copper wheel rotating at a linear velocity of 52 $m^{-1}s$. According to the empirical formula proposed by William Johnson,[27] $R_c = dT/dt$ (K/s) = $10/D^2$ (cm), the cooling rate was estimated to be between 1.6-2.1 × $10^6$ K $s^{-1}$. The density of these alloys was measured using the Archimedes method. Over five tests for each batch of alloy were conducted to ensure accuracy and consistency. The average value of these measurements was taken as the density of the alloys. The density of the designed alloys was between 7.738 and 7.789 g $cm^{-3}$. The measurement uncertainty in Bs, caused by density measurements, was ≈±0.03 T. The

*Structural Characterization*: The amorphous structure of the as-quenched ribbon samples was identified by XRD (Bruker D8 ADVANCE) with the Cu-K$\alpha$ radiation. Magnetic-field-assisted heat treatment was

made at 340–420 °C for 15 mins. The samples were annealed in a tubular annealing furnace with a vacuum of $5 \times 10^{-3}$ Pa. The microstructure of annealed alloys was investigated by TEM (Talos F200X) The TEM samples were prepared by the Focused Ion Beam (FIB, Carl Zeiss Auriga).

*Magnetic Property Tests*: The $B_s$ of the ribbons were measured by using a vibrating sample magnetometer (VSM, Lake Shore 7410) at a maximum magnetic field of 800 kA $m^{-1}$ (10 kOe). The $H_c$ of the ribbons was measured by DC B-H tracers (Linkjoin MATS-2010SD) at a magnetic field of 800 A $m^{-1}$.

*First Principles Calculation*: Using VASP,[28] quenched amorphous alloy formation was simulated via ab initio molecular dynamics. Starting with a $Fe_{23}B_6$ crystal structure from the Materials Project.[29] Expand it fourfold to obtain a $Fe_{92}B_{24}$ supercell. Two or Four boron atoms were substituted with Zr, Nb, Mo, Al, Ga, or Si to change the alloy's $\delta_\chi$. The structure was then optimized in the NPT ensemble using a conjugate gradient algorithm for rationality. This was followed by molecular dynamics simulations in the NVT ensemble, involving melting the alloy at 3000 K for 2 ps, cooling from 3000 K to 1300 K over 1 ps, stabilizing at 1300 K for 1 ps, and quenching to 300 K at a $2 \times 10^{14}$ K $s^{-1}$ rate in 6ps. The amorphous alloys were subjected to structural relaxation after quenching to ensure a more rational configuration of the amorphous structure. Finally, a two-step static calculation was performed, self-consistent and non-self-consistent, to determine the total magnetic moment and density of states of the alloy.

In all computational processes, electron interactions were characterized using the Perdew-Burke-Ernzerhof (PBE) functional,[30] a refinement of the Generalized Gradient Approximation (GGA) for exchange-correlation. Given the sufficient size of the supercell, only the Gamma point was considered in the Brillouin zone. All molecular dynamics simulations employed a Nosé–Hoover thermostat to control temperature.[31] Both the structural optimization and magnetic calculations took into account electron spin polarization.

## Supporting Information

Supporting Information is available from the Wiley Online Library or from the author.

## Acknowledgements

The authors acknowledge the financial supports from the National Key R&D Program of China (2024YFB3813700), National Natural Science Foundation of China (NSFC 52231006, 52001319, 92163108, 52271158, 52222105, 51827801, 52201194), Zhejiang Provincial Natural Science Foundation of China (LGF22E010002, LZ22A030001, LR22E010004), "Pioneer, Leading Goose" R&D Program of Zhejiang (2022C01023), and Ningbo Key Scientific, Technological Project (2019B10051). The authors appreciate the help from Professor Qiang Luo and Professor Baolong Shen in the annealing experiment and the discussion with Dr. Peiheng Jiang and Professor Zhicheng Zhong in the *ab initial* simulations.

## Conflict of Interest

The authors declare no conflict of interest.

## Author Contributions

S.Y. and B.Z. contribute equally to this work. J.-Q.W. and J.H. designed and supervised the project. S.Y. performed this research. B.Z. and F.S. provided experimental guidance and assistance. All authors participated in the discussion of the results and contributed to the preparation of the manuscript.

## Data Availability Statement

The data that support the findings of this study are available from the corresponding author upon reasonable request.

## Keywords

amorphous materials, artificial intelligence, high magnetization, low coercivity, nanocrystalline alloys

Received: December 24, 2024
Revised: February 14, 2025
Published online:

[1] J. M. Silveyra, E. Ferrara, D. L. Huber, T. C. Monson, *Science* **2018**, *362*, 418.
[2] B. K. Bose, *Ieee Ind. Electron. M* **2010**, *4*, 6.
[3] G. Herzer, *Acta. Mater.* **2013**, *61*, 718.
[4] K. F. Yao, L. X. Shi, S. Q. Chen, Y. Shao, N. Chen, J. L. Jia, *Acta. Phys. Sin-Ch Ed.* **2018**, *67*, 016101.
[5] A. M. Leary, P. R. Ohodnicki, M. E. McHenry, *Jom-Us* **2012**, *64*, 772.
[6] Y. Meng, S. Pang, C. Chang, G. Wang, H. Li, T. Zhang, *J. Mater. Res. Technol.* **2022**, *20*, 161.
[7] F. Shen, B. Zang, L. Song, J. Huo, Y. Zhang, J.-Q. Wang, *Scripta. Mater.* **2023**, *236*, 115666.
[8] a) T. N. G. Li, Y. H. Li, L. C. Wu, L. Qi, W. Zhang, *J. Alloy Compd.* **2022**, *918*, 165735; b) Z. X. Huo, G. Q. Zhang, J. H. Han, J. P. Wang, S. Ma, H. T. Wang, *Processes* **2022**, 10.
[9] a) A. Agrawal, A. Choudhary, *APL Mater.* **2016**, *4*, 053208; b) T. Mueller, A. G. Kusne, R. Ramprasad, *Rev. Comp. Ch.* **2016**, *29*, 186; c) A. Merchant, S. Batzner, S. S. Schoenholz, M. Aykol, G. Cheon, E. D. Cubuk, *Nature* **2023**, *624*, 80.
[10] a) W. J. Huang, P. Martin, H. L. L. Zhuang, *Acta. Mater.* **2019**, *169*, 225; b) J. Xiong, S.-Q. Shi, T.-Y. Zhang, *Mater. Des.* **2020**, *187*, 108378; c) Y. Wang, Y. Tian, T. Kirk, O. Laris, J. H. Ross, R. D. Noebe, V. Keylin, R. Arróyave, *Acta. Mater.* **2020**, *194*, 144; d) F. Ren, L. Ward, T. Williams, K. J. Laws, C. Wolverton, J. Hattrick-Simpers, A. Mehta, *Sci. Adv.* **2018**, *4*, 1566. e) Z. Rao, P.-Y. Tung, R. Xie, Y. Wei, H. Zhang, A. Ferrari, T. P. C. Klaver, F. Körmann, P. T. Sukumar, A. Kwiatkowski da Silva, Y. Chen, Z. Li, D. Ponge, J. Neugebauer, O. Gutfleisch, S. Bauer, D. Raabe, *Science* **2022**, *378*, 78.
[11] S. M. Lundberg, G. Erion, H. Chen, A. DeGrave, J. M. Prutkin, B. Nair, R. Katz, J. Himmelfarb, N. Bansal, S. I. Lee, *Nat. Mach. Intell.* **2020**, *2*, 56.
[12] L. Ward, A. Dunn, A. Faghaninia, N. E. R. Zimmermann, S. Bajaj, Q. Wang, J. Montoya, J. Chen, K. Bystrom, M. Dylla, K. Chard, M. Asta, K. A. Persson, G. J. Snyder, I. Foster, A. Jain, *Comput. Mater. Sci.* **2018**, *152*, 60.
[13] G. Zhong, L.-N. Wang, X. Ling, J. Dong, *J. Fin. Data Sci.* **2016**, *2*, 265.
[14] J. Cai, J. Luo, S. Wang, S. Yang, *Neurocomputing* **2018**, *300*, 70.
[15] T. Q. Chen, C. Guestrin, *Kdd'16: Proceedings of the 22nd Acm Sigkdd Int. Conf. on Knowledge Discovery and Data Mining*, Association for Computing Machinery (ACM), San Francisco, CA, USA **2016**.
[16] L. Breiman, *Mach. Learn.* **2001**, *45*, 5.
[17] S. F. Ding, Z. B. Zhu, X. K. Zhang, *Neural. Comput. Appl.* **2017**, *28*, 969.
[18] C. Strobl, A.-L. Boulesteix, A. Zeileis, T. Hothorn, *BMC Bioinformatics* **2007**, *8*, 25.
[19] A. Altmann, L. Toloşi, O. Sander, T. Lengauer, *Bioinformatics* **2010**, *26*, 1340.
[20] S. M. Lundberg, S.-I. Lee, in *Proceedings of the 31st International Conference on Neural Information Processing Systems*, Curran Associates Inc., Long Beach, California, USA **2017**, 4768.
[21] A. Inoue, *Acta Mater.* **2000**, *48*, 279.
[22] A. P. Srivastava, in *Handbook of Materials Science*, (Eds: R. S. Ningthoujam, A. K. Tyagi), Springer Nature Singapore, Singapore **2024**, Vol. *2*, 293.

 

[23] a) X. S. Li, J. Zhou, L. Q. Shen, B. A. Sun, H. Y. Bai, W. H. Wang, *Adv. Mater.* **2022**, *35*, 2205863; b) L. Hou, M. Li, C. Jiang, X. Fan, Q. Luo, S. Chen, P. Song, W. Li, *J. Alloy. Compd.* **2021**, *853*, 157071; c) H. Zheng, L. Zhu, S. S. Jiang, Y. G. Wang, S. N. Liu, S. Lan, F. G. Chen, *J. Alloy. Compd.* **2020**, *816*, 152549.

[24] Q. Luo, D. Li, M. Cai, S. Di, Z. Zhang, Q. Zeng, Q. Wang, B. Shen, *J. Mater. Sci. Technol.* **2022**, *116*, 72.

[25] a) K. Suzuki, A. Makino, N. Kataoka, A. Inoue, T. Masumoto, *Mater. Transact. Jim* **1991**, *32*, 93; b) Y. Yoshizawa, S. Oguma, K. Yamauchi, *J. Appl. Phys.* **1988**, *64*, 6044; c) J. Zhou, J. You, K. Qiu, *J. Appl. Phys.* **2022**, *132*, 040702; d) Y. Yoshizawa, *Scripta. Mater.* **2001**, *44*, 1321; e) A. Makino, T. Bitoh, A. Kojima, A. Inoue, T. Masumoto, *J. Magn. Magn. Mater.* **2000**, *215*, 288; f) T. Bitoh, M. Nakazawa, A. Makino, A. Inoue, T. Masumoto, *J. Appl. Phys.* **1999**, *85*, 5127; g) Y. Yoshizawa, *Advances in Nanocrystallization* **1999**, *307*, 51; h) A. Makino, T. Hatanai, A. Inoue, T. Masumoto, *Mat. Sci. Eng. a-Struct.* **1997**, *226*, 594; i) A. Inoue, A. Makino, T. Masumoto, *Mater. Sci. Forum* **1995**, *179*, 497; j) K. Suzuki, A. Makino, A. Inoue, T. Masumoto, *J. Appl. Phys.* **1993**, *74*, 3316; k) M. A. Willard, D. E. Laughlin, M. E. McHenry, D. Thoma, K. Sickafus, J. O. Cross, V. G. Harris, *J. Appl. Phys.* **1998**, *84*, 6773; l) Y. Yoshizawa, *Mater. Sci. Forum* **1999**, *307*, 51.

[26] F. Pedregosa, G. Varoquaux, A. Gramfort, V. Michel, B. Thirion, O. Grisel, M. Blondel, P. Prettenhofer, R. Weiss, V. Dubourg, J. Vanderplas, A. Passos, D. Cournapeau, M. Brucher, M. Perrot, E. Duchesnay, *J. Mach. Learn Res.* **2011**, *12*, 2825.

[27] X. H. Lin, W. L. Johnson, *J. Appl. Phys.* **1995**, *78*, 6514.

[28] G. Kresse, J. Furthmuller, *Comput. Mater. Sci.* **1996**, *6*, 15.

[29] A. Jain, O. Shyue Ping, G. Hautier, W. Chen, W. D. Richards, S. Dacek, S. Cholia, D. Gunter, D. Skinner, G. Ceder, K. A. Persson, *APL Mater.* **2013**, *1*, 011002.

[30] J. P. Perdew, K. Burke, M. Ernzerhof, *Phys. Rev. Lett.* **1997**, *78*, 1396.

[31] S. Nose, *Mol. Phys.* **1984**, *52*, 255.